

# A Robust Point Matching Algorithm for Autoradiograph Alignment

Anand Rangarajan<sup>1</sup>, Haili Chui<sup>2</sup>, Eric Mjolsness<sup>4</sup>, Suguna Pappu<sup>1</sup>, Lila Davachi<sup>3</sup>, Patricia S. Goldman-Rakic<sup>3</sup> and James S. Duncan<sup>1,2</sup>

Department of <sup>1</sup>Diagnostic Radiology, <sup>2</sup>Department of Electrical Engineering and  
<sup>3</sup>Section of Neurobiology,  
Yale University

<sup>2</sup>Department of Computer Science and Engineering  
University of California San Diego (UCSD)

## Abstract

We present a novel method for the geometric alignment of autoradiographs of the brain. The method is based on finding the spatial mapping and the one-to-one correspondences (or homologies) between point features extracted from the images and rejecting non-homologies as outliers. In this way, we attempt to account for the local natural and artifactual differences between the autoradiograph slices. We have executed the resulting automated algorithm on a set of left prefrontal cortex autoradiograph slices, specifically demonstrated its ability to perform point outlier rejection, validated it using synthetically generated spatial mappings and provided a visual comparison against the well known iterated closest point (ICP) algorithm. Visualization of a stack of aligned left prefrontal cortex autoradiograph slices is also provided.

## 1 Introduction

Neuroimaging of the human brain has opened the way for a genuine understanding of human cognition; but the circuitry and cellular basis of the extraordinary information processing capacity of humans can be addressed only in experimental animals such as nonhuman primates. Current research in nonhuman primates (Friedman and Goldman-Rakic, 1994) is concerned with elucidating functional maps of cortical activity using the 2-deoxyglucose (2-DG) autoradiographic method developed by (Sokoloff et al., 1977). This method requires sacrifice of the animal and sectioning of the brain into serial sections followed by production of thousands of autoradiographs of individual brain sections.

One current downside of analyzing these autoradiographs, however, are the very large amounts of data that are produced. Each one of four sections of a monkey brain that are typically analyzed may be used to generate 1000 individual brain slices which are themselves not in register. While the spatial resolution of the individual 2-D slices is very high, the 3-D spatial structure available for example in volumetric MRI is lost. Consequently, sequential alignment of autoradiograph slices is not sufficient for 3-D reconstruction [or “reconstitution” (Kim et al., 1995)]. Since we have access to functional (metabolic)

2-DG autoradiographs and 3-D MRI of the same primate, we divide autoradiograph reconstitution into two stages: i) 2-D alignment of the autoradiograph slices and ii) 3-D non-rigid registration of the slices with 3-D MRI.

In this paper, we present a solution to the first problem by designing a new automated autoradiograph alignment method. The method is based on a newly developed *robust point matching* (RPM) algorithm (Rangarajan et al., 1996; Gold et al., 1995) that simultaneously finds homologies (correspondences) and similarity transformation parameters (rotation, translation and scale) between sequential pairwise slices. The inability of previous automated autoradiograph alignment methods to correct for artifacts like cuts and tears in the slices and for systematic variation from slice to slice is hereby accounted for. Our method is somewhat robust to this variability in the statistical sense of rejecting artifacts and natural differences as *outliers*—point features in either slice that have no homologies in the other slice (Black and Rangarajan, 1996). And central to our method is a novel approach to the problem of determining unique point-to-point correspondences (homologies) while rejecting outliers or non-homologies.

We formulate the problem of alignment as a mixed variable (binary and continuous) optimization problem: the binary variables are the point correspondences and the continuous variables are the spatial mapping parameters (rotation, translation and scale). Correspondence is parameterized as a permutation. Parameterized in this manner, for any fixed value of the spatial mapping parameters, the correspondence problem is mapped into the *linear assignment* problem (Bertsekas and Tsitsiklis, 1989) results. The *softassign*, a new technique that first arose in the neural computation literature (Rangarajan et al., 1996; Kosowsky and Yuille, 1994), has been shown to find the optimum solution to the assignment problem when embedded in a *deterministic annealing* scheme. When the correspondence variables are frozen, a standard least-squares problem results which can be efficiently solved for the spatial mapping parameters. The RPM algorithm essentially iterates between solving for the spatial mapping and the correspondence variables at each setting of the temperature (in deterministic annealing). The preceding is a slight simplification: correspondence is never a permutation due to the presence of outliers. The softassign within deterministic annealing performs outlier rejection in addition to assigning the point correspondences.

## 2 Previous Work

Automated autoradiograph alignment is the primary goal of this paper and we present our new alignment method in Section 3. If previous automated methods achieve autoradiograph alignment, why do we require another method? The *principal flaw* that other point feature based methods share in comparison to the RPM method is that they are not robust (Black and Rangarajan, 1996) in the statistical sense of automatically accounting for some of the cuts, tears and natural variations between slices via the mechanism of outlier rejection.

The principal autoradiograph alignment methods are i) principal axis/center of mass (Hibbard and Hawkins, 1988), ii) frequency domain cross correlation (Toga and Banerjee, 1993), iii) spatial domain cross correlation (Toga and Banerjee, 1993; van den Elsen et al., 1993) and iv) the disparity analysis (Zhao et al., 1993) methods. The principal axis method detects the center of mass of the two images, translates one image so that the center of masses coincide, then finds the principal axes using the eigenvector transform and aligns them via a rotation. The method is not robust to tears in the slices and also does not perform well when the images do not have bilateral symmetry. Cross correlation methods (either frequency or spatial domain) maximize the cross correlation with respect to the transformation parameters. This approach assumes densitometric consistency between slices. Consequently, the method is not robust to changes in the intensity patterns and when cuts and tears are present in the slices. A good comparison of these methods can be found in (Toga and Banerjee, 1993). The disparity analysis method is based on optical flow. An affine transformation is used to regularize the flow field at each point. The method works with either boundary or intensity information. Consequently, the method is dependent either on good boundary detection or on densitometric consistency and is not robust.

There are a huge number of image matching methods [see (van den Elsen et al., 1993) for an excellent review]. Most of these methods directly compare image intensities. For example, the Automated Image Registration (AIR) method of (Woods et al., 1993) is based on comparing intensity values between MR and PET in similar tissue volumes. The sums of the standard deviations of the PET intensities associated with a particular MR value are minimized w.r.t. the spatial transformation. Assessing robustness of voxel based schemes is not straightforward and consequently it is not clear how this (and other voxel based ) approaches perform relative to recent point feature based methods.

Another image intensity based matching measure is deterministic/stochastic sign change (D/SSC) (Venot and Leclerc, 1984). In DSC, a periodic intensity pattern is added to one image and for the current placement of the template image, the total number of sign changes in the difference image scanned line by line is counted. This measure is maximized w.r.t the spatial mapping. SSC is a stochastic variant of DSC wherein a Poisson noise pattern is substituted for the periodic pattern (Hoh et al., 1993). The resulting “objective functions may not be smooth and therefore hard to optimize” (Buzug et al., 1996).

Mutual information and joint entropy based measures have recently become very popular due to the wide applicability of the method (Collignon et al., 1995; Hill et al., 1994; Viola and Wells, 1995). These are pixel and voxel similarity methods that are based on estimating the joint probability of the reference and target image (under the current spatial transformation) either using the joint histogram or through statistical nonparametric methods such as Parzen windows. These methods are quite robust to noise and other differences between the images. As in the case of (Woods et al., 1993) above, it is not clear how these methods compare with our approach.

In addition to image intensity matching methods, there are an enormous number of point feature

(edge, ridge/ravine etc.) matching algorithms in the literature. For example, point matching algorithms that seek rigid transformations have been designed by minimizing the Hausdorff distance between point sets (Huttenlocher et al., 1993). The Hausdorff distance is the distance to the nearest point of the most mismatched point in either point set [ $H(A, B) = \max(h(A, B), h(B, A))$  where  $h(A, B) = \max_{a \in A} \min_{b \in B} \|a - b\|$ . Here  $A$  and  $B$  are two point sets]. While this method can reject large numbers of point outliers, it does not have a noise model which hampers its performance in the face of both point “jitter” and point outliers.

A popular parametric point correspondence method is chamfer matching (van den Elsen et al., 1993; Borgefors, 1988; Jiang et al., 1992). In chamfer matching, a distance image is obtained by calculating the Euclidean distance from each pixel to the nearest edge (point) feature. The pixels “hit” by the current location of the template are used to compute the chamfer distance—essentially the root-mean-squared of the distance image pixels encountered by the template. While recent efforts have improved its robustness properties, the method is prone to local minima due to the brittleness of the nearest neighbor measure. It is available as part of ANALYZE, a popular medical image analysis software package from the Mayo clinic (Robb and Hanson, 1991).

Other discrete search methods have been tried for point matching with varying degrees of success. These can be classified under i) tree searches, ii) Hough transforms, iii) geometric hashing and iv) the alignment method. Tree search methods involve searching over a tree of possible matches while eliminating branches of the tree from consideration (Baird, 1984; Grimson and Lozano-Perez, 1987; Umeyama, 1993). The generalized Hough transform divides the valid set of spatial mappings into discrete bins. Good matches are registered as votes in the appropriate bin (Ballard, 1981; Stockman, 1987). In geometric hashing, depending on the spatial mapping, a set of possible bases that can represent the point sets is generated. Then a voting based search is conducted to determine the point to point correspondences (Lamdan et al., 1988; Hummel and Wolfson, 1988). In the alignment method (Ullman, 1989), each alignment feature (defined as a set of three distinctive points) in the image is matched against each alignment feature in the model. The best spatial mapping from all such possible mappings is chosen. More recently, probabilistic techniques have been applied to enhance the speed of this alignment method (Olson, 1995). Most of these discrete search methods are not robust to missing/spurious points and noise and to variations in the number of voting bins.

Techniques more closely related to ours are approaches based on nonlinear optimization and neural networks, eigenvector based approaches, and relaxation labeling. Within the neural network community, nonlinear optimization approaches have been attempted to formulate and solve the point matching problem (Yuille, 1990; Mjolsness and Garrett, 1990; Hinton et al., 1992; Gee et al., 1993; Vinod and Ghose, 1993; Lu and Mjolsness, 1994). Typically, an objective function which handles both the spatial mapping and correspondence is minimized. However, none of these methods explicitly handled the problem of ensuring one-to-one point correspondences while rejecting outliers. This is a constraint that a point in

one set can match to only one point in the other set. For example, in (Hinton et al., 1992), an objective function with affine and correspondence parameters was minimized but only a one-way matching constraint was imposed. Similar problems related to constraint satisfaction beset the objective function based methods of (Vinod and Ghose, 1993; Gee et al., 1993). Turning to eigenvector based approaches, (Scott and Longuet-Higgins, 1991) have a formulation for point matching with a matrix that indicates matches and a proximity matrix whose elements are the pairwise distance between points. The proximity matrix is a function of a Gaussian weighted distance metric, with a parameter  $\sigma$  controlling the degree of interaction between the two sets of features. Their eigenvector based approach computes the modes of the proximity matrix, and they show that for a large enough value of  $\sigma$ , they recover the correct global correspondence. (Shapiro and Brady, 1992) continue this work by including modal shape information to address the weaknesses of (Scott and Longuet-Higgins, 1991)'s algorithm, primarily its inability to recover large rotations in the transformations, and also algorithmic instabilities at large values of  $\sigma$ . Relaxation labeling algorithms first introduced by (Ranade and Rosenfeld, 1980) have also been widely applied to point matching. However these methods were originally developed as tools for classification and consequently in general do not impose the one-to-one matching constraints required in correspondence problems. (Ton and Jain, 1989) attempt to impose such a matching constraint within the relaxation labeling framework with limited success. (Li, 1992) uses a form of deterministic annealing (graduated non-convexity) within the relaxation labeling framework, but once again only with a one-way matching constraint.

Finally, noteworthy for its thoroughgoing approach is the iterated closest point algorithm (ICP) of (Besl and McKay, 1992). This method is based on minimizing the distances between points in one set and the closest point in the other set with respect to the spatial transformation. The point features are not restricted to just edge features and can run the gamut of points, lines, curves, and surfaces. However, the reliance on finding the closest point makes the distance measure brittle, sensitive to changes in feature location and to false positives in the detection of closest points. This problem is partially alleviated in (Feldmar and Ayache, 1996) by using an adaptive threshold to decide whether the closest point is a homology or an outlier. The threshold depends on the variance of the minimum distances found in each iteration. A direct anecdotal visual comparison between ICP (in the above enhanced mode) and RPM is presented in Section 4.

Having cursorily examined other general image matching and point matching methods in the literature, we now turn to our approach. It should be fairly obvious after reviewing our criticism of the other approaches that our approach relies on robust matching of edge features while handling one-to-one correspondences in a non-brittle manner.

### 3 Automated Autoradiograph Alignment Approach

We now describe the methodology for the alignment of the 2-D autoradiograph slices. A characteristic feature of the autoradiograph slices that are adjacent is overall similarity except for local areas of dissimilarity. Cuts, tears, irregular slicing and natural variations create local deformations from slice to slice. Since the slices are handled individually, there is a fairly significant change in orientation between adjacent slices. For all these reasons and others mentioned in Section 2, there is a need for a robust image matching method that finds similarity transformations (rotation, translation, scale) between slices and is somewhat stable to local deformations. Such an algorithm is the RPM method and as we shall demonstrate, there is great synergy in applying this method to our problem. Previous work (Gold et al., 1995; Rangarajan et al., 1996) with the RPM algorithm was confined to data generated synthetically or at best handwritten characters. There is no prior work detailing use of an edge detector to get point features followed by the RPM method.

Assume that the edge detection phase is completed and we have edge images corresponding to the autoradiograph slices. [As we shall describe later, a Canny edge detector (Canny, 1986) is sufficient to obtain edges with good localization.] High confidence edges alone are chosen after thresholding the edge images. The locations corresponding to the edges are then obtained from the edge images. Denote the edge location information from slice 1 and slice 2,  $X_i$ ,  $i = 1, 2, \dots, N_1$  and  $Y_j$ ,  $j = 1, 2, \dots, N_2$  respectively.  $N_1$  and  $N_2$  are the numbers of edge locations in the sets  $X$  and  $Y$  respectively. The RPM algorithm minimizes the following objective function:

$$\begin{aligned} \min_{M, \theta, t, s} E(M, \theta, t, s) &= \sum_{i=1}^{N_1} \sum_{j=1}^{N_2} M_{ij} \|X_i - t - sR(\theta)Y_j\|^2 + \frac{\gamma}{2} (\log s)^2 - \alpha \sum_{i=1}^{N_1} \sum_{j=1}^{N_2} M_{ij} \\ \text{subject to } \sum_{i=1}^{N_1+1} M_{ij} &= 1, \forall j \in \{1, \dots, N_2\}, \sum_{j=1}^{N_2+1} M_{ij} = 1, \forall i \in \{1, \dots, N_1\} \text{ and } M_{ij} \in \{0, 1\}. \end{aligned} \quad (1)$$

Equation (1) describes an optimization problem from which the transformation parameters—rotation angle  $\theta$ , translation  $t$ , and scale  $s$ —can be obtained by minimization. In (1),  $\gamma$  is a regularization parameter which controls the degree of departure of the scale parameter from unity. However, (1) also sets up an optimization problem on the point correspondences. A set of correspondence variables  $\{M_{ij}\}$ —the *match matrix*—has been defined such that:

$$M_{ij} = \begin{cases} 1 & \text{if point } X_i \text{ corresponds to point } Y_j \\ 0 & \text{otherwise,} \end{cases}$$

and

$$M_{i(N_2+1)} = \begin{cases} 1 & \text{if point } X_i \text{ is an outlier} \\ 0 & \text{otherwise} \end{cases}, \quad M_{(N_1+1)j} = \begin{cases} 1 & \text{if point } Y_j \text{ is an outlier} \\ 0 & \text{otherwise.} \end{cases}$$

The variable  $M_{ij}$  is a correspondence variable which indicates when homologies have been found or outliers discarded. If  $M_{ij}$  is one (for  $i$  or  $j$  not equal to  $N_1 + 1$  or  $N_2 + 1$  respectively), feature “ $i$ ” in slice

1 and feature “ $j$ ” in slice 2 are homologies. The constraints on  $M_{ij}$  enforce one-to-one correspondence between homologies and also robustness (Black and Rangarajan, 1996): a point feature in one image may have no corresponding homology and is discarded as an outlier. The degree of robustness is enforced by the parameter  $\alpha$ . If  $\alpha$  is large, fewer points are discarded and vice-versa. This technique is closely related to the robust statistics approach based on M-estimators and influence functions (Black and Rangarajan, 1996). Automatically finding homologies is important because of the time consuming and labor intensive nature of manual selection. Automatically discarding features that have no homologies is important—otherwise the method would suffer from the same problems that beset intensity correlation.

As mentioned previously, the above optimization problem in (1) contains two interlocking optimization problems—one on the spatial mapping between the two slices and the other on the point-to-point feature correspondences between the two slices. When the edge feature correspondences are known, a constrained least squares problem results from which the similarity transformation is obtained. When the spatial mapping (a similarity transformation in this case) is known, we obtain a linear assignment problem (Bertsekas and Tsitsiklis, 1989). (The presence of outliers makes our problem slightly different from the traditional linear assignment problem.) While polynomial time linear assignment algorithms exist in the literature, we’ll describe a new algorithm that is better suited to interact with the constrained least squares solution to the spatial mapping. The result is a two stage algorithm which alternates between solving for the spatial mapping and the correspondences.

The main difficulty in jointly solving for the spatial mapping and the correspondences lies in the seemingly disparate natures of the two problems, one continuous, the other combinatorial. Our approach is designed to overcome this problem. First, ignore the effect of outliers on the match matrix in (1). The match matrix then becomes a *permutation matrix* with binary entries and all rows and columns summing to one. Then we invoke the Birkhoff-von Neumann theorem which states that “the set of  $(N \times N)$  doubly stochastic matrices is the convex hull of the set of  $(N \times N)$  permutation matrices” (Kosowsky and Yuille, 1994). A doubly stochastic matrix is a square matrix with all positive entries and rows and columns summing to one. In other words, permutation matrices (or the permutation group) are the vertices of an  $N$  dimensional doubly stochastic polytope. Consequently, the linear assignment problem can be solved by linear programming and related interior-point methods which relax the constraint that the match matrix entries be binary and merely require them to be positive. Due to the linear objective, the solution always occurs at a vertex of the doubly stochastic polytope—a permutation matrix. Following the Birkhoff-von-Neumann theorem, we relax the match matrix constraints from permutation matrix constraints to doubly stochastic matrix constraints. Doubly stochastic matrix constraints require positivity of each match matrix entry with rows and columns summing to one. We enforce the row and column constraints using Lagrange parameters and the positivity constraint via a *barrier function* (Luenberger, 1984):

$$E(M, \theta, t, s, \mu, \nu) = \sum_{i=1}^{N_1} \sum_{j=1}^{N_2} M_{ij} \|X_i - t - sR(\theta)Y_j\|^2 + \frac{\gamma}{2} (\log s)^2 - \alpha \sum_{i=1}^{N_1} \sum_{j=1}^{N_2} M_{ij}$$

$$+ \sum_{i=1}^{N_1} \mu_i \left( \sum_{j=1}^{N_2+1} M_{ij} - 1 \right) + \sum_{j=1}^{N_2} \nu_j \left( \sum_{i=1}^{N_1+1} M_{ij} - 1 \right) + \frac{1}{\beta} \sum_{i=1}^{N_1+1} \sum_{j=1}^{N_2+1} M_{ij} \log M_{ij}. \quad (2)$$

In (2),  $\mu$  and  $\nu$  are two Lagrange parameters enforcing the row and column constraints respectively. Note that the two Lagrange parameters  $\mu$  and  $\nu$  do not force the outlier row  $\{M_{(N_1+1)j}\}$  or column  $\{M_{i(N_2+1)}\}$  to sum to one.  $\beta > 0$  is the control parameter of the  $x \log x$  entropy barrier function (Rangarajan et al., 1996; Gold and Rangarajan, 1996; Yuille and Kosowsky, 1994) which enforces the positivity constraint. We have transformed the original mixed continuous-combinatorial optimization problem into a nonlinear optimization problem.

Fixing the spatial mapping, we can solve for the match matrix  $M$  in the above objective function. Minimizing (2) w.r.t.  $M$ , we get

$$M_{ij} = \exp \left[ -\beta \left( \|X_i - t - sR(\theta)Y_j\|^2 - \alpha + \mu_i + \nu_j \right) - 1 \right], \quad \forall i \in \{1, \dots, N_1\}, \quad \forall j \in \{1, \dots, N_2\}.$$

$$M_{i(N_2+1)} = \exp(-\beta\mu_i - 1), \quad \forall i \in \{1, \dots, N_1\}, \quad M_{(N_1+1)j} = \exp(-\beta\nu_j - 1), \quad \forall j \in \{1, \dots, N_2\}. \quad (3)$$

In (3),  $\beta$  is held fixed and we have yet to determine the two Lagrange parameters  $\mu$  and  $\nu$  which are required to satisfy the row and column constraints. The exponentiation in (3) keeps all the match matrix entries positive and is a consequence of using the  $x \log x$  barrier function. Solving for the two Lagrange parameters using a gradient ascent approach is likely to be slow and inefficient. Fortunately, the row and column constraints in (1) and (3) can be efficiently solved using a remarkable theorem due to Sinkhorn (Sinkhorn, 1964): A doubly stochastic matrix is obtained from any square matrix with positive entries by the simple process of alternating row and column normalizations. While it may appear that Sinkhorn’s theorem is unrelated to the two Lagrange parameters  $\mu$  and  $\nu$ , this is not the case. Solving for the Lagrange parameters by alternating between solving for  $\mu$  and then  $\nu$  rather than steepest ascent is *identical* to Sinkhorn’s algorithm (except for the added benefit of the outliers) (Rangarajan et al., 1996). Note that Sinkhorn’s procedure returns a doubly stochastic matrix with all rows and columns summing to one. Solving for the Lagrange parameters in (2) results in an algorithm which alternately normalizes all rows and columns *except* for the outlier row and column. With  $\beta$  held fixed, the exponentiation in (3) followed by Sinkhorn’s algorithm yields a doubly stochastic matrix as expected. Slowly increasing  $\beta$  results in a permutation matrix and the optimal solution to the linear assignment problem (Kosowsky and Yuille, 1994; Rangarajan et al., 1996; Gold and Rangarajan, 1996). Since the exponentiation and Sinkhorn’s algorithm at fixed  $\beta$  is central to our approach, we refer to this as the *softassign*. Due to its similarity to simulated annealing, we refer to the barrier function control parameter  $\beta$  as the *inverse temperature*.  $\beta$  is slowly increased according to an annealing schedule. As the deterministic annealing parameter  $\beta$  is increased, the match matrix entries “harden”—they approach binary values. Outlier rejection occurs in the limit when  $\beta \rightarrow \infty$  with the outliers becoming binary valued. Since the entire process is deterministic, we refer to the overall approach as deterministic annealing. Deterministic annealing has been shown to avoid poor local minima (Rangarajan et al., 1996) which is especially important since outlier rejection



almost always generates local minima (Black and Rangarajan, 1996).

The spatial mapping parameters are updated with the match matrix held fixed. Closed-form solutions are obtained for the rotation and translation parameters by equating to zero the partial derivatives of  $E(M, \theta, t, s)$  w.r.t. to each parameter. The scale parameter is set using a few iterations of Newton's method; whenever the regularization parameter  $\gamma$  is set to zero, we use the closed-form solution [obtained by equating to zero the partial derivative of  $E(M, \theta, t, s)$  w.r.t. to the scale parameter]. While it is possible to simultaneously solve for the rotation and translation parameters using a 2-D version of the quaternion approach in (Walker et al., 1991), we have not done so here. Variable and constant definitions can be found in Table 1. The pseudocode describes the RPM algorithm in minute detail.

### The Robust Point Matching (RPM) Algorithm

**Initialize**  $\theta, t$  to zero,  $s$  to one,  $\beta$  to  $\beta_0$  and  $M_{ij}$  to  $1 + \epsilon_{ij}$

**Begin A: Deterministic Annealing.** Do A until  $\beta \geq \beta_f$

**Begin B:** Do B until  $M$  converges or # of iterations  $> I_0$

**Begin C: Softassign.**

For all  $i \in \{1, \dots, N_1\}$  and  $j \in \{1, \dots, N_2\}$

$$Q_{ij} \leftarrow -\|X_i - t - sR(\theta)Y_j\|^2 + \alpha$$

$$M_{ij} \leftarrow \exp(\beta Q_{ij})$$

**Begin D: Sinkhorn.** Do D until  $M$  converges or # of iterations  $> I_1$

Update  $M$  by normalizing the rows (except the outlier row):

$$M_{ij} \leftarrow \frac{M_{ij}}{\sum_{j=1}^{N_2+1} M_{ij}}, \quad i \in \{1, \dots, N_1\}, \quad j \in \{1, \dots, N_2 + 1\}$$

Update  $M$  by normalizing the columns (except the outlier column):

$$M_{ij} \leftarrow \frac{M_{ij}}{\sum_{i=1}^{N_1+1} M_{ij}}, \quad i \in \{1, \dots, N_1 + 1\}, \quad j \in \{1, \dots, N_2\}$$

**End D**

**End C**

**Begin E: Spatial mapping update.**

Update  $\theta$  using analytical solution

Update  $t$  using analytical solution

Update  $s$  using Newton's method

**End E**

**End B**

$$\beta \leftarrow \beta_r \beta$$

**End A**

$\beta$	control parameter of the deterministic annealing method
$\beta_0$	initial value of the control parameter $\beta$
$\beta_f$	maximum value of the control parameter $\beta$
$\beta_r$	rate at which the control parameter $\beta$ is increased
$\{\epsilon_{ij}\}$	small positive random variable
$\{M_{ij}\}$	match matrix variables including outliers
$\{Q_{ij}\}$	squared Euclidean distance between point $i$ and $j$
$I_0$	maximum # of iterations allowed at each value of the control parameter, $\beta$
$I_1$	maximum # of iterations allowed for Sinkhorn's method (back and forth row and column normalizations)

Table 1: Variable and constant definitions for the robust point matching algorithm

## 4 Results

Having described the method in general, we now apply it to two autoradiograph slices (405 and 409) of the left prefrontal cortex shown in Figure 1. First we run a Canny edge detector (Canny, 1986) on each slice. The edge detector uses a single scale Gaussian filter with width  $\sigma$  and incorporates hysteresis and non-maximum suppression. Low  $t_l$  and high  $t_h$  threshold parameters can be specified for edge tracking. The parameters used for both slices were— $\sigma = 1.5$ ,  $t_l = 2$  and  $t_h = 255$ . The edge images shown in Figure 2. Some gradations in edge strength are discernible from the edge images. We now threshold the edge images to obtain binary images: the same threshold of 240 was chosen for both slices. Then the point sets shown in Figure 3 are obtained from the binary images. There were 976 and 1505 points in the point-sets corresponding to slices 405 and 409 respectively. We then cluster the point-sets using a method described below to reduce the point count. This is preferable to randomly choosing a fraction of the points. The clustered point-sets shown in Figure 4 have 61 and 76 points corresponding to slices 405 and 409 respectively.

Having obtained the point sets, we now execute the RPM algorithm. Exactly as described above, we specify an initial value for the continuation parameter  $\beta_0 = 1/10000$ . The robustness parameter  $\alpha$  was set to 5. A linear schedule was prescribed for  $\beta$ ;  $\beta_r = \frac{\beta^{(n)}}{\beta^{(n+1)}} = 0.93$ . The scale regularization parameter  $\gamma$  was set to  $\frac{4}{\beta}$ . The maximum number of Sinkhorn iterations was 30. At each setting of  $\beta$ , we executed the inner loop of the algorithm a maximum of 10 times. Initial conditions and the registration results are shown in Figure 5 for the two cases of the scale parameter turned off and turned on. The results show that a good spatial mapping is discovered when the scale parameter is turned off since in this case, the scale parameter does not interfere with outlier rejection. When the scale parameter is present, a somewhat

suboptimal registration is obtained.

In the above experiment, we presented an anecdotal study of the accuracy of the RPM algorithm. Obviously, the speed and convergence properties of the algorithm are important issues as well. The RPM algorithm has a complexity (Gold et al., 1995) of  $O(N_1 N_2)$  where  $N_1$  and  $N_2$  are the numbers of points in each point set. The current speed of our implementation is about 1-2 minutes for 100 points on a Silicon Graphics Indigo2 workstation with a R10000 processor. We have already seen that edge feature extraction typically results in a point count much greater than 100 points. The overall speed and accuracy can be dramatically improved by embedding the RPM algorithm in a multi-grid scheme.

We have experimented with one particular multi-grid scheme based on clustering the point-sets. If the size of the original image is  $M_1 \times M_2$ , a sequence of smaller image *sizes* is generated by dividing by powers of two. If the image size cannot be further divided, an extra row or column is added prior to division. For example, if the original image size is  $973 \times 1019$ , the sequence is  $974 \times 1020$ ,  $487 \times 510$ ,  $244 \times 255$ ,  $122 \times 128$ ,  $61 \times 64$ ,  $31 \times 32$ ,  $16 \times 16$  etc. At each level, the original points are clustered by computing the centroid of the points that fall into the larger pixel of that level. It is now possible to track the parent/children relationships of the points across levels. The RPM algorithm is then executed beginning with the point-set at a coarse level and the temperature set to  $T_0 = \frac{1}{\beta_0}$ . When the temperature reaches  $\frac{T_0}{2}$ , the new point-set at the next finer level is loaded and the process repeated. This method of setting the temperature was determined experimentally. Since the correspondences have not yet reached binary values, we equally divide the parent<sub>X</sub> – parent<sub>Y</sub> correspondence among the cross-product of all the children of the next stage. For example, if point  $i$  in  $X$  has 3 children and point  $j$  has 4, we create a new, larger match matrix by dividing the correspondence entry  $M_{ij}$  by 12. The outlier variables pick up the slack and ensure that all rows and columns sum to one, except for the outlier row and column.

In the following experiments, this clustering scheme was used. Figure 6 shows the autoradiograph slices 360, 363, 384 and 415 of the left prefrontal cortex. A different digitization scheme was used resulting in slices of higher spatial resolution ( $\simeq 20\mu n$ ) than the autoradiograph slices shown in Figure 1. The corresponding Canny edge images shown in Figure 7, mainly feature the boundaries of the two images. The point-sets generated by clustering autoradiograph slice 360 are shown in Figure 8. The point count at levels 1, 2, 4, 8, 16, 32, 64 and 128 are 4971, 2637, 1351, 669, 327, 152, 68 and 26 respectively. Initial conditions and the obtained registrations are shown in Figure 9. with the depicted point sets corresponding to a stopping level of 16. The recovered registration parameters are shown in Table 2. In these experiments, the following parameter values were used: edge detection parameter  $\sigma = 1.5$ , low edge detection threshold  $t_l = 2$ , high edge detection threshold  $t_h = 255$ , edge discretization threshold of 240, robustness parameter  $\alpha = 5$ , scale regularization parameter  $\gamma = \frac{4}{\beta}$ , initial temperature  $T_0 = \frac{1}{\beta_0} = 10000$ , number of iterations at each temperature  $I_0 = 10$ , maximum number of Sinkhorn iterations  $I_1 = 30$ , and annealing schedule  $\beta_r = \frac{1}{0.93}$ . We started at level 128 stopping at level 16.

Table 2: Registration parameters found by RPM.

Slices	Rotation (in degrees)	Translation (in pixels)	Scale
405-409	13.6	[-1.3,-26.7]	1
405-409 <sup>1</sup>	12.8	[15.9,0]	0.887
360-363	4.9	[40.4,51.4]	0.984
360-384	42.9	[339.5,-77.4]	0.956
360-415	20.7	[-62.7,207.3]	0.950
363-384	-48.5	[-137,354]	0.926

The next experiment showcases the robustness property. We matched slices 363 and 384 at level 64 with 84 and 58 points respectively. We changed the edge detection parameters to obtain an edge image for slice 363 with more internal detail resulting in a point-set shown in Figure 10 with many internal points. We ran the single level RPM algorithm and the results are shown in Figure 10. Despite the large rotation and the differences in point count, the RPM algorithm was able to match the outer contour. Careful examination of the right edge of the registration plot shown on the bottom right of Figure 10 reveals a somewhat imperfect match between the two contours there.

Validation of the RPM algorithm was performed using autoradiograph slice 360 and synthetically generated transformation parameters. 100 points were obtained from slice 360. The point-set was isotropically scaled to fit inside a unit square. In each trial, a “jittered” point-set was created by adding independent Gaussian noise  $N(0, \sigma)$  to each point. Then a fraction  $p_d$  of the points were deleted and another fraction  $p_s$  of random, spuriously generated points in the unit square were added. Finally, a randomly generated transformation was applied to the point-set. The RPM algorithm was then executed to find the correspondence and the spatial mapping between the two point-sets. 30 trials were run at each standard deviation and for each combination of  $p_d$  and  $p_s$ . The following parameter values were used: robustness parameter  $\alpha = 5$ , initial temperature  $T_0 = 0.005$ , scale regularization parameter  $\gamma = \frac{4}{\beta}$ , number of iterations at each temperature  $I_0 = 10$ , maximum number of Sinkhorn iterations  $I_1 = 30$ , and annealing schedule  $\beta_r = \frac{1}{0.93}$ .

The transformation parameters  $\{t_x, t_y, \theta, s\}$  were bounded in the following way:  $-0.5 < t_x, t_y < 0.5$ ,  $-27^\circ < \theta < 27^\circ$ ,  $0.5 < s < 2$ . Each parameter was chosen independently and uniformly from the possible ranges.

We used the error measure  $e_\tau = 3 \left| \frac{\tau^{\text{actual}} - \tau^{\text{estimated}}}{\tau^{\text{range}}} \right|$  where  $e_\tau$  is the error measure for parameter  $\tau$  (rotation, translation or scale) and  $\tau^{\text{range}}$  is the aforementioned range of permissible values of  $\tau$ . Dividing by  $\tau^{\text{range}}$  is preferable to dividing by  $\tau^{\text{actual}}$  since the latter inappropriately weights small  $\tau^{\text{actual}}$  values.

<sup>1</sup>This example was run twice with and without the scale parameter turned on.

The reported error (ordinate in Figure 11) is the average error over all three parameters.

Next we compared RPM with the well known iterated closest point (ICP) algorithm (Besl and McKay, 1992; Feldmar and Ayache, 1996). We used the following energy function for ICP:<sup>2</sup>

$$E_{\text{icp}}(\theta, t, s) = \sum_{i=1}^{N_1} u_i \min_j \|X_i - t - sR(\theta)Y_j\|^2 + \sum_{j=1}^{N_2} v_j \min_i \|X_i - t - sR(\theta)Y_j\|^2 \quad (4)$$

where

$$\begin{aligned} u_i &= \begin{cases} 1 & \text{if } \min_j \|X_i - t - sR(\theta)Y_j\|^2 < u_{\text{thr}} \\ 0 & \text{if } \min_j \|X_i - t - sR(\theta)Y_j\|^2 \geq u_{\text{thr}} \end{cases} \\ v_j &= \begin{cases} 1 & \text{if } \min_i \|X_i - t - sR(\theta)Y_j\|^2 < v_{\text{thr}} \\ 0 & \text{if } \min_i \|X_i - t - sR(\theta)Y_j\|^2 \geq v_{\text{thr}} \end{cases} \end{aligned} \quad (5)$$

with  $u_{\text{thr}} = K\sigma_1$ , and  $v_{\text{thr}} = K\sigma_2$ .  $\sigma_1$  and  $\sigma_2$  are the variances of the minimum distances  $\min_j \|X_i - t - sR(\theta)Y_j\|$  and  $\min_i \|X_i - t - sR(\theta)Y_j\|$  respectively.  $K$  was always set to 2.

The ICP energy function was minimized by coordinate-descent using closed-form solutions for each parameter. To ensure a fair comparison, the RPM algorithm used a closed-form solution for the scale parameter as well. No regularization term was used for the scale parameter.

We compared the two algorithms on autoradiograph slices 360-363 and 360-384 as shown in Figures 12 and 13. Approximately 150 points were generated from the edge detector outputs by clustering. The results show that RPM and ICP give similar results when the problem instance is not very difficult as shown in Figure 12. However, for a larger value of rotation, ICP had difficulty finding close to optimum results. On the other hand, RPM came close to finding a good solution. ICP can be approximately seen as a zero temperature version of our algorithm. Indeed, at zero temperature, the correspondence engine in RPM reduces to finding the nearest point and rejecting outliers beyond a threshold.

Finally, we executed the multi-grid RPM algorithm on a stack of 37 left prefrontal cortex autoradiograph slices beginning with slice 339 and ending with slice 460. Many slices in between had to be discarded prior to digitization due to their poor quality. The stack is visualized in Figure 14 in three orientations. An oblique cut through the principal sulcus region shows some visual conformity. The need for non-rigid registration of the slices is evident from the local deformations seen in the visualization.

## 5 Discussion

We have investigated some of the properties of the RPM algorithm. The context has been mostly autoradiograph alignment, but we have also provided experimental benchmarks in the case of known, synthetically generated spatial mappings as shown in Figure 11. Inspection of Figure 11 suggests that

---

<sup>2</sup>We acknowledge one anonymous reviewer for this particular formulation of ICP.

the performance of RPM shows graceful degradation with changes along the orthogonal dimensions of noise and percentage of outliers. Anecdotal studies have also been conducted to demonstrate the robustness property (Figure 10) and to compare RPM with ICP—a closely related point matching algorithm (Figures 12 and 13).

Several issues remain undecided. We have not investigated the variation in performance with respect to the robustness parameter, the scale regularization parameter, the annealing schedule and level of discretization of the edges. For instance, we have noticed a relatively stable change in behavior for values of  $\alpha$  in the range of 0-10 but obviously more studies need to be performed. Likewise, the effect of varying the scale regularization parameter has not been studied. We have noticed that setting  $\gamma$  to zero does not seem to create any unusual problems but there are definitely situations where it is preferable to have some regularization. The annealing schedule and level of discretization are least problematic. We have already shown in Figure 10 that RPM performs well even when there are a number of outliers present in one image. This circumvents the problem of edge discretization somewhat. The capture range especially for rotation and scale is an even more important issue. From experimental evidence alone, we concluded that a range of about  $54^\circ$  for  $\theta$  and a range of 4 for  $s$  was appropriate for our synthetically generated statistical benchmarks (Figure 11). The difficulty for analysis here is that RPM being a deterministic annealing method forgets initial conditions if the starting temperature is high enough. Consequently, large rotations in excess of  $50^\circ$  are sometimes recovered if the initial descent w.r.t.  $\theta$  is in the correct direction. Our overall experience with deterministic annealing is that poor local minima are avoided but the global minimum is not necessarily found. This is another issue that deserves further investigation.

Finally, we have not addressed the larger issue of comparison with voxel based methods. Like RPM, ICP is a point matching method facilitating straightforward comparison. It would be interesting to compare RPM with either AIR (Woods et al., 1993) or the mutual information approach (Viola and Wells, 1995).

## 6 Conclusion

We have developed a new automated autoradiograph alignment method which is based on Canny edge detection followed by a robust point matching (RPM) algorithm that solves for a similarity transformation between slices. The method automatically finds homologies or corresponding features, and rejects non-homologies as outliers. The alignment method is the first stage in a two stage procedure that i) aligns sequential, pairwise autoradiograph slices and ii) registers and warps the autoradiograph volume onto 3-D MRI. While we have not discussed registration with MRI in this paper, it plays a crucial role in lending 3-D volumetric coherence to the process of autoradiograph reconstitution. Finally, the automated alignment method presented here can be applied to other areas such as registration of MRI to anatomical atlases, and to intermodality registration in general.

## Acknowledgements

We thank the reviewers (two in particular) for their numerous comments, suggestions and criticisms. This project is partially supported by a grant from the Whitaker Foundation to Anand Rangarajan. We also thank Gene Gindi, Steven Gold and Hemant Tagare for helpful comments and Jim Rambo for his help in visualizing the stack of autoradiographs.

## References

- Baird, H. (1984). *Model-Based Image Matching Using Location*. MIT Press, Cambridge, MA.
- Ballard, D. H. (1981). Generalized Hough transform to detect arbitrary patterns. *IEEE Trans. Patt. Anal. Mach. Intell.*, 13(2):111–122.
- Bertsekas, D. P. and Tsitsiklis, J. N. (1989). *Parallel and Distributed Computation: Numerical Methods*. Prentice-Hall, Englewood Cliffs, NJ.
- Besl, P. J. and McKay, N. D. (1992). A Method for Registration of 3-D Shapes. *IEEE Trans. Patt. Anal. Mach. Intell.*, 14(2):239–256.
- Black, M. and Rangarajan, A. (1996). On the Unification of Line Processes, Outlier Detection and Robust Statistics with Applications in Early Vision. *Intl. J. Computer Vision*, 19(1):57–91.
- Borgefors, G. (1988). Hierarchical chamfer matching: a parametric edge matching algorithm. *IEEE Trans. Patt. Anal. Mach. Intell.*, 10(6):849–865.
- Buzug, T. M., Weese, J., Fassnacht, C., and Lorenz, C. (1996). Using an entropy similarity measure to enhance the quality of DSA images with an algorithm based on template matching. In Hohne, K. H. and Kikinis, R., editors, *Visualization in Biomedical Computing*, volume 1131 of *Lecture notes in Computer Science*, pages 235–240. Springer-Verlag.
- Canny, J. (1986). A Computational Approach to Edge Detection. *IEEE Trans. on Pattern Analysis and Machine Intelligence*, 8(6):679–698.
- Collignon, A., Vandermeulen, D., Suetens, P., and Marchal, G. (1995). 3D multi-modality medical image registration using feature space clustering. In Ayache, N., editor, *Computer Vision, Virtual Reality and Robotics in Medicine*, volume 905 of *Lecture Notes in Computer Science*, pages 195–204. Springer-Verlag.
- Feldmar, J. and Ayache, N. (1996). Rigid, Affine and Locally Affine Registration of Free-Form Surfaces. *Intl. J. Computer Vision*, 18(2):99–119.

- Friedman, H. R. and Goldman-Rakic, P. S. (1994). Coactivation of Prefrontal Cortex and Inferior Parietal Cortex in Working Memory Tasks Revealed by 2DG Functional Mapping in the Rhesus Monkey. *J. Neuroscience*, 14(5):2775–2788.
- Gee, A. H., Aiyer, S., and Prager, R. W. (1993). An analytical framework for optimizing neural networks. *Neural Networks*, 6:79–97.
- Gold, S., Lu, C. P., Rangarajan, A., Pappu, S., and Mjolsness, E. (1995). New Algorithms for 2-D and 3-D Point Matching: Pose Estimation and Correspondence. In Tesauro, G., Touretzky, D., and Alspector, J., editors, *Advances in Neural Information Processing Systems 7*, pages 957–964. MIT Press, Cambridge, MA.
- Gold, S. and Rangarajan, A. (1996). A graduated assignment algorithm for graph matching. *IEEE Transactions on Pattern Analysis and Machine Intelligence*, 18(4):377–388.
- Grimson, E. and Lozano-Perez, T. (1987). Localizing overlapping parts by searching the interpretation tree. *IEEE Trans. Patt. Anal. Mach. Intell.*, 9:468–482.
- Hibbard, L. S. and Hawkins, R. A. (1988). Objective Image Alignment for Three-Dimensional Reconstruction of Digital Autoradiograms. *J. Neurosci. Methods*, 26:55–75.
- Hill, D., Studholme, C., and Hawkes, D. (1994). Voxel Similarity Measures for Automated Image Registration. In *Proc. Third Conf. Visualization in Biomedical Computing*, pages 205–216.
- Hinton, G., Williams, C., and Revow, M. (1992). Adaptive elastic models for hand-printed character recognition. In Moody, J., Hanson, S., and Lippmann, R., editors, *Advances in Neural Information Processing Systems 4*, pages 512–519. Morgan Kaufmann, San Mateo, CA.
- Hoh, C. K., Dahlbom, M., Harris, G., Choi, Y., Hawkins, R. A., Phelps, M. E., and Maddahi, J. (1993). Automated iterative three-dimensional registration of positron emission tomography images. *J. Nucl. Med.*, 34(11):2009–18.
- Hummel, R. and Wolfson, H. (1988). Affine invariant matching. In *Proceedings of the DARPA Image Understanding Workshop*, pages 351–364, Cambridge, MA.
- Huttenlocher, D. P., Klanderman, G. A., and Rucklidge, W. J. (1993). Comparing images using the Hausdorff distance. *IEEE Trans. Patt. Anal. Mach. Intell.*, 15(9):850–863.
- Jiang, H., Robb, R. A., and Holton, K. S. (1992). A new approach to 3-D registration of multimodality medical images by surface matching. In *Visualization in Biomedical Computing*, volume SPIE vol. 1808, pages 196–213.



- Kim, B., Frey, K. A., Mukhopadhyay, S., Ross, B. D., and Meyer, C. R. (1995). Co-Registration of MRI and Autoradiography of Rat Brain in Three-Dimensions following Automatic Reconstruction of 2-D data set. In Ayache, N., editor, *Computer Vision, Virtual Reality and Robotics in Medicine*, volume 905 of *Lecture Notes in Computer Science*, pages 262–271. Springer-Verlag.
- Kosowsky, J. J. and Yuille, A. L. (1994). The invisible hand algorithm: Solving the assignment problem with statistical physics. *Neural Networks*, 7(3):477–490.
- Lamdan, Y., Schwartz, J., and Wolfson, H. (1988). Object recognition by affine invariant matching. *IEEE Conf. Comp. Vision, Patt. Recog.*, pages 335–344.
- Li, S. Z. (1992). Matching: invariant to translations, rotations and scale changes. *Pattern Recognition*, 25:583–594.
- Lu, C. P. and Mjolsness, E. (1994). Two-dimensional object localization by coarse-to-fine correlation matching. In Cowan, J., Tesauro, G., and Alspector, J., editors, *Advances in Neural Information Processing Systems 6*. Morgan Kaufmann, San Francisco, CA.
- Luenberger, D. (1984). *Linear and Nonlinear Programming*. Addison-Wesley, Reading, MA.
- Mjolsness, E. and Garrett, C. (1990). Algebraic transformations of objective functions. *Neural Networks*, 3:651–669.
- Olson, C. F. (1995). Probabilistic indexing for object recognition. *IEEE Trans. Patt. Anal. Mach. Intell.*, 17(5):518–521.
- Ranade, S. and Rosenfeld, A. (1980). Point pattern matching by relaxation. *Pattern Recognition*, 12:269–275.
- Rangarajan, A., Gold, S., and Mjolsness, E. (1996). A novel optimizing network architecture with applications. *Neural Computation*, 8(5):1041–1060.
- Robb, R. A. and Hanson, D. P. (1991). A software system for interactive and quantitative visualization of multidimensional biomedical images. *Australas Phys. Eng. Sci. Med.*, 14:9–30.
- Scott, G. and Longuet-Higgins, C. (1991). An algorithm for associating the features of two images. *Proc. Royal Society of London*, B244:21–26.
- Shapiro, L. and Brady, J. (1992). Feature-based correspondence: an eigenvector approach. *Image and Vision Computing*, 10:283–288.
- Sinkhorn, R. (1964). A relationship between arbitrary positive matrices and doubly stochastic matrices. *Ann. Math. Statist.*, 35:876–879.

- Sokoloff, L., Revich, M., Kennedy, C., DesRosiers, M. H., Patlak, C. S., Pettigrew, K. D., Sakurada, O., and Shinohara, M. (1977). The  $^{14}\text{C}$ -deoxyglucose method for the measurement of local cerebral glucose utilization: theory, procedure, and normal values in the conscious and anesthetized albino rat. *J. Neurochem.*, 28:897–916.
- Stockman, G. (1987). Object recognition and localization via pose clustering. *Computer Vision, Graphics, and Image Processing*, 40:361–387.
- Toga, A. W. and Banerjee, P. K. (1993). Registration revisited. *J. Neurosci. methods*, 48:1–13.
- Ton, J. and Jain, A. (1989). Registering Landsat images by point matching. *IEEE Trans. Geo. Rem. Sens.*, 27(5):642–651.
- Ullman, S. (1989). Aligning pictorial descriptions: An approach to object recognition. *Cognition*, 32(3):193–254.
- Umeyama, S. (1993). Parameterized point pattern matching and its application to recognition of object families. *IEEE Trans. Patt. Anal. Mach. Intell.*, 15(1):136–144.
- van den Elsen, P., Pol, E., and Viergever, M. (1993). Medical image matching—A review with classification. *IEEE Engineering in Medicine and Biology*, 12:26–39.
- Venot, A. and Leclerc, V. (1984). Automated correction of patient motion and grey values prior to subtraction in digitized angiography. *IEEE Trans. Med. Imag.*, 3(4):179–186.
- Vinod, V. and Ghose, S. (1993). Point matching using asymmetric neural networks. *Pattern Recognition*, 26:1207–1214.
- Viola, P. and Wells, W. M. (1995). Alignment by Maximization of Mutual Information. In *Fifth International Conference on Computer Vision and Pattern Recognition (ICCV)*, pages 16–23. IEEE Press.
- Walker, M. W., Shao, L., and Volz, R. (1991). Estimating 3-D location parameters using dual number quaternions. *CVGIP: Image Understanding*, 54(3):358–367.
- Woods, R. P., Mazziotta, J. C., and Cherry, S. R. (1993). MRI–PET registration with automated algorithm. *J. Computer Assisted Tomography*, 17(4):536–546.
- Yuille, A. L. (1990). Generalized deformable models, statistical physics, and matching problems. *Neural Computation*, 2(1):1–24.
- Yuille, A. L. and Kosowsky, J. J. (1994). Statistical physics algorithms that converge. *Neural Computation*, 6(3):341–356.

Zhao, W., Young, T. Y., and Ginsberg, M. D. (1993). Registration and Three-Dimensional Reconstruction of Autoradiographic Images by the Disparity Analysis Method. *IEEE Transactions on Medical Imaging*, 12(4):782–791.

### List of Figures

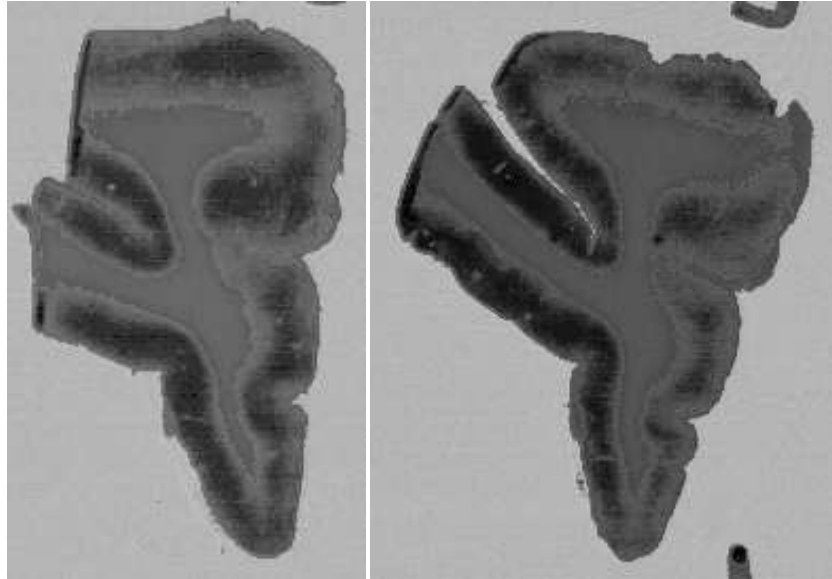


Figure 1: Autoradiograph slices of the left prefrontal cortex. Left: Slice 405. Right: Slice 409.

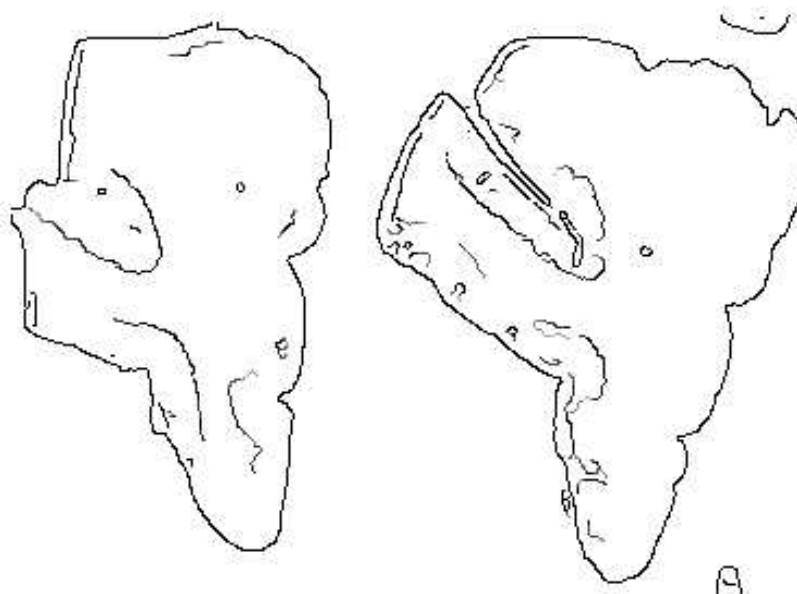


Figure 2: Canny edge images corresponding to the autoradiograph slices 405 and 409.

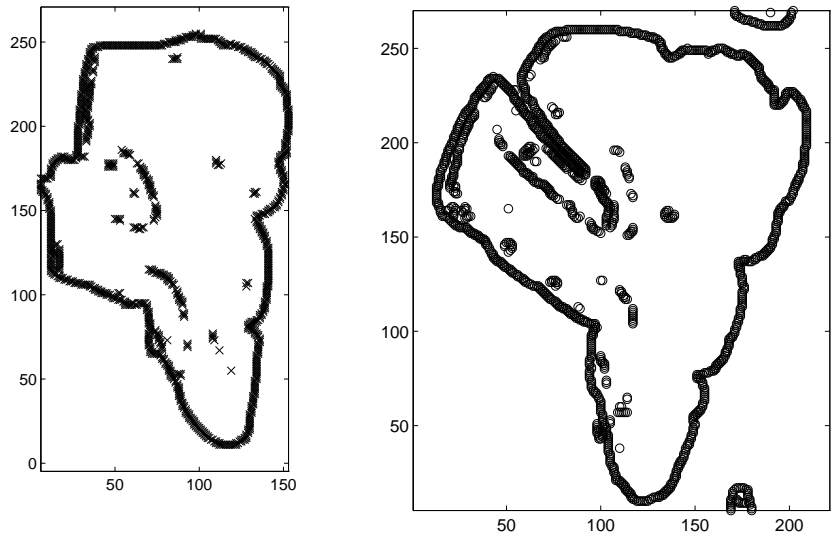


Figure 3: Point sets corresponding to the Canny edge images.

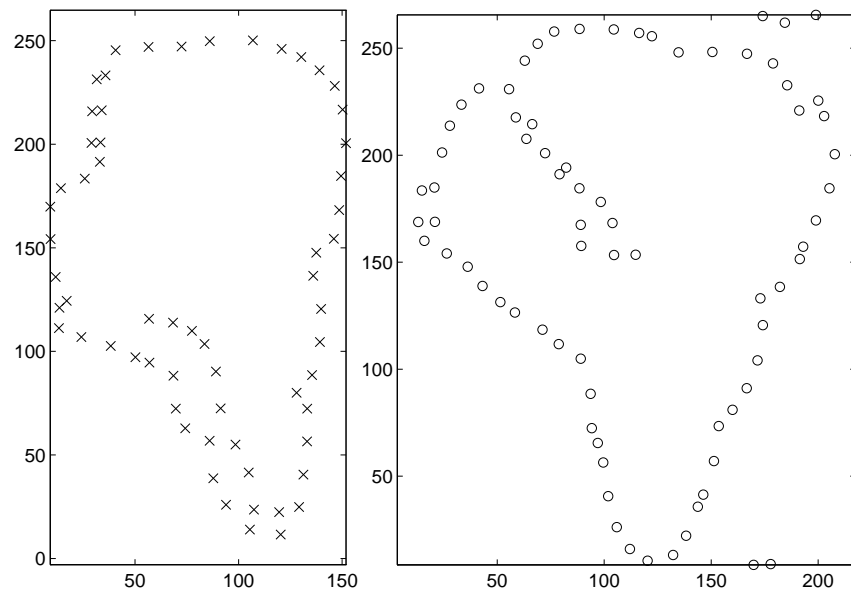


Figure 4: Clustered point sets.

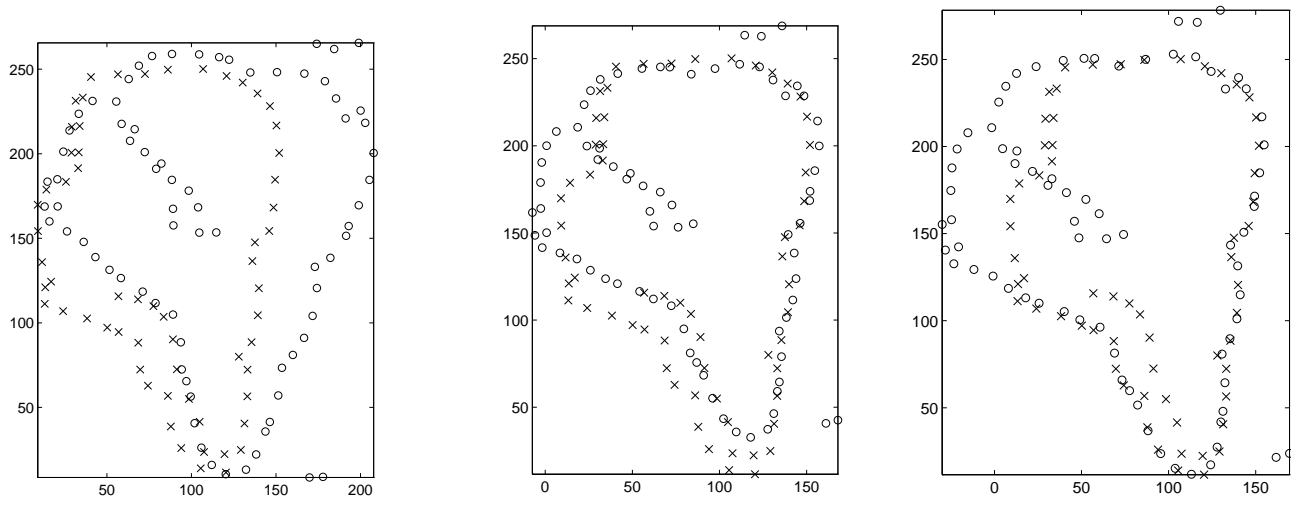


Figure 5: Left: Initial condition. Center: RPM solution with scale parameter. Right: RPM solution without scale parameter.

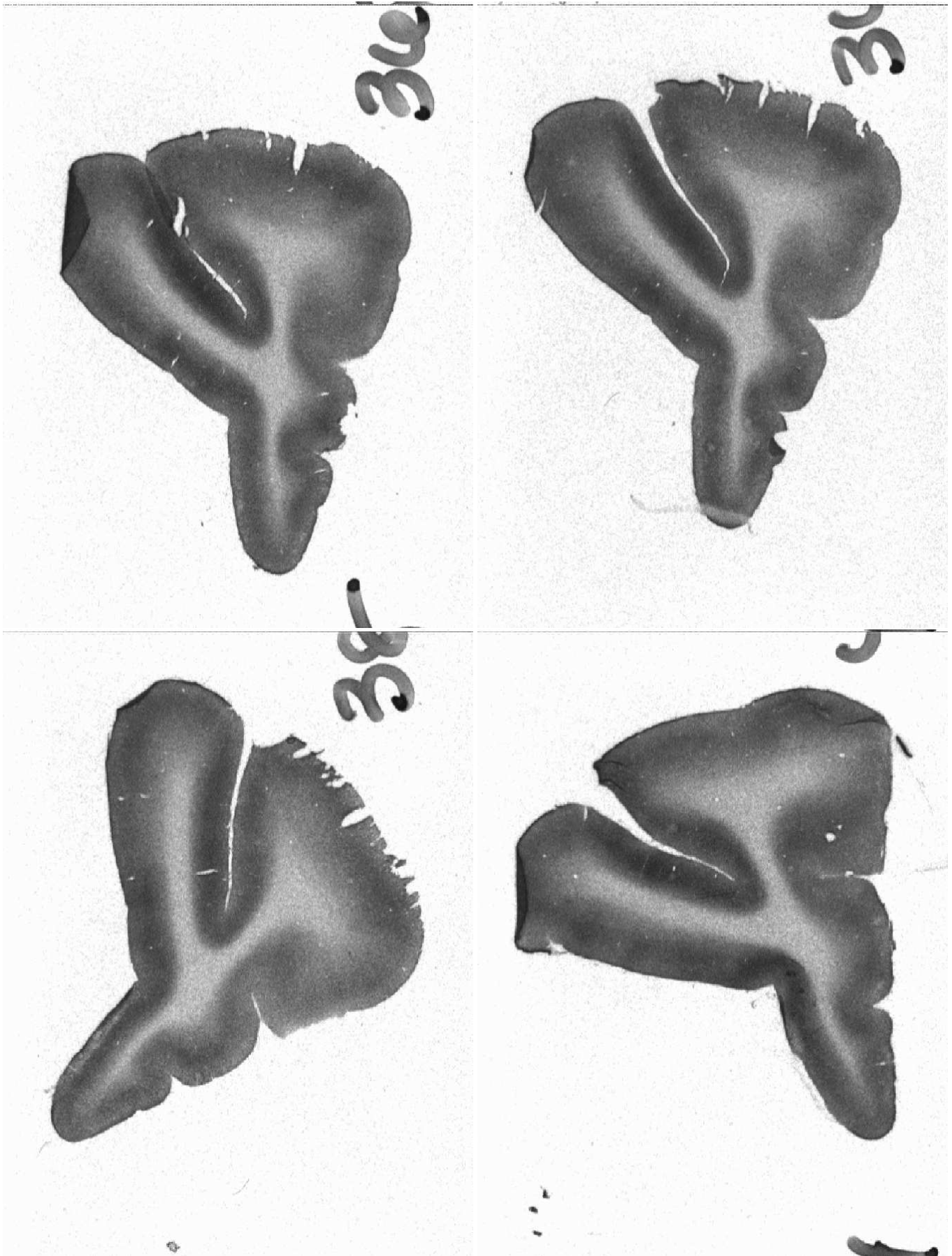


Figure 6: Autoradiograph slices corresponding to the left prefrontal cortex. Top Left: Slice 360. Top Right: Slice 363. Bottom Left: Slice 384. Bottom Right: Slice 415.

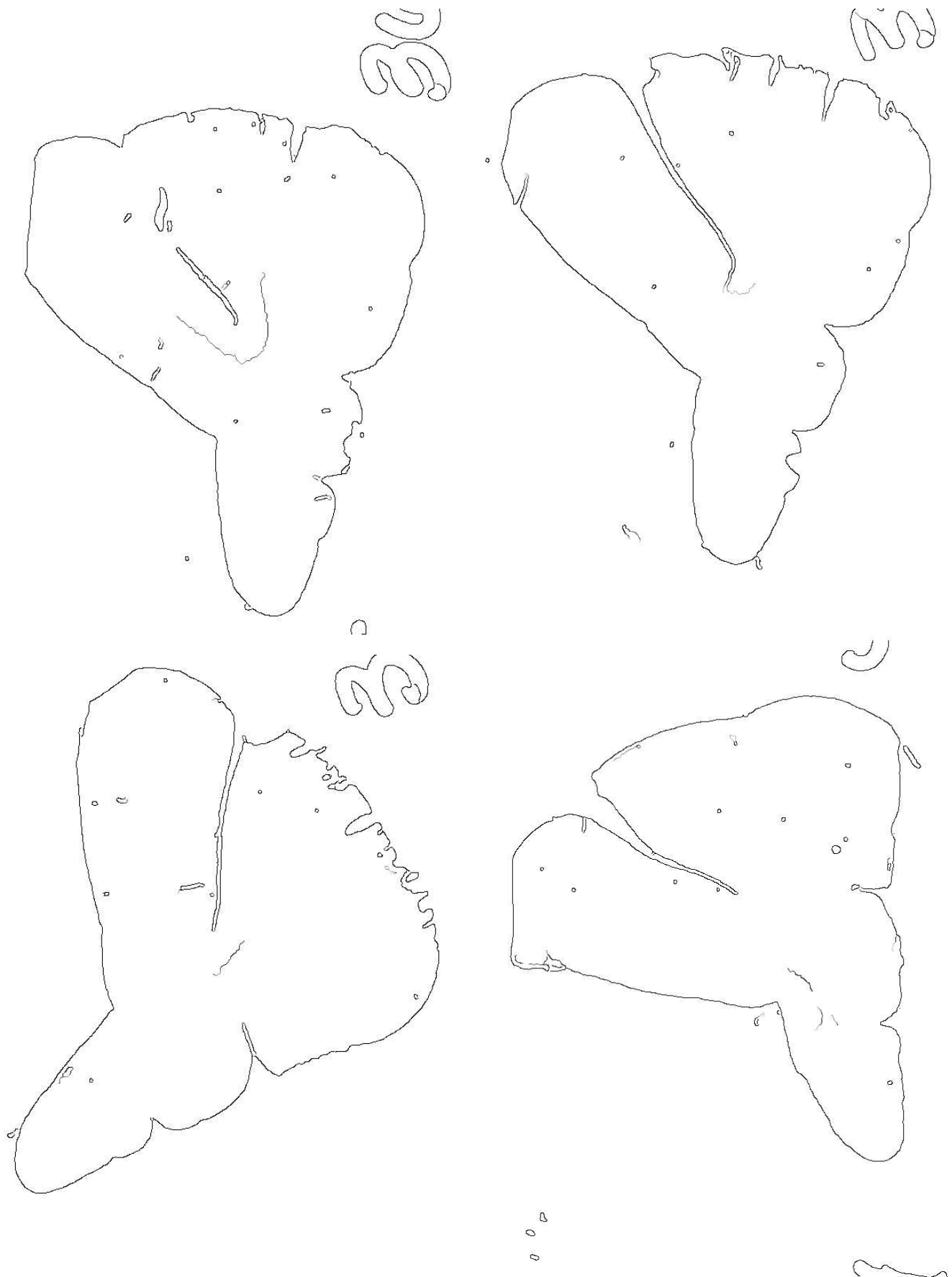


Figure 7: Canny edge images corresponding to the autoradiograph slices shown above.

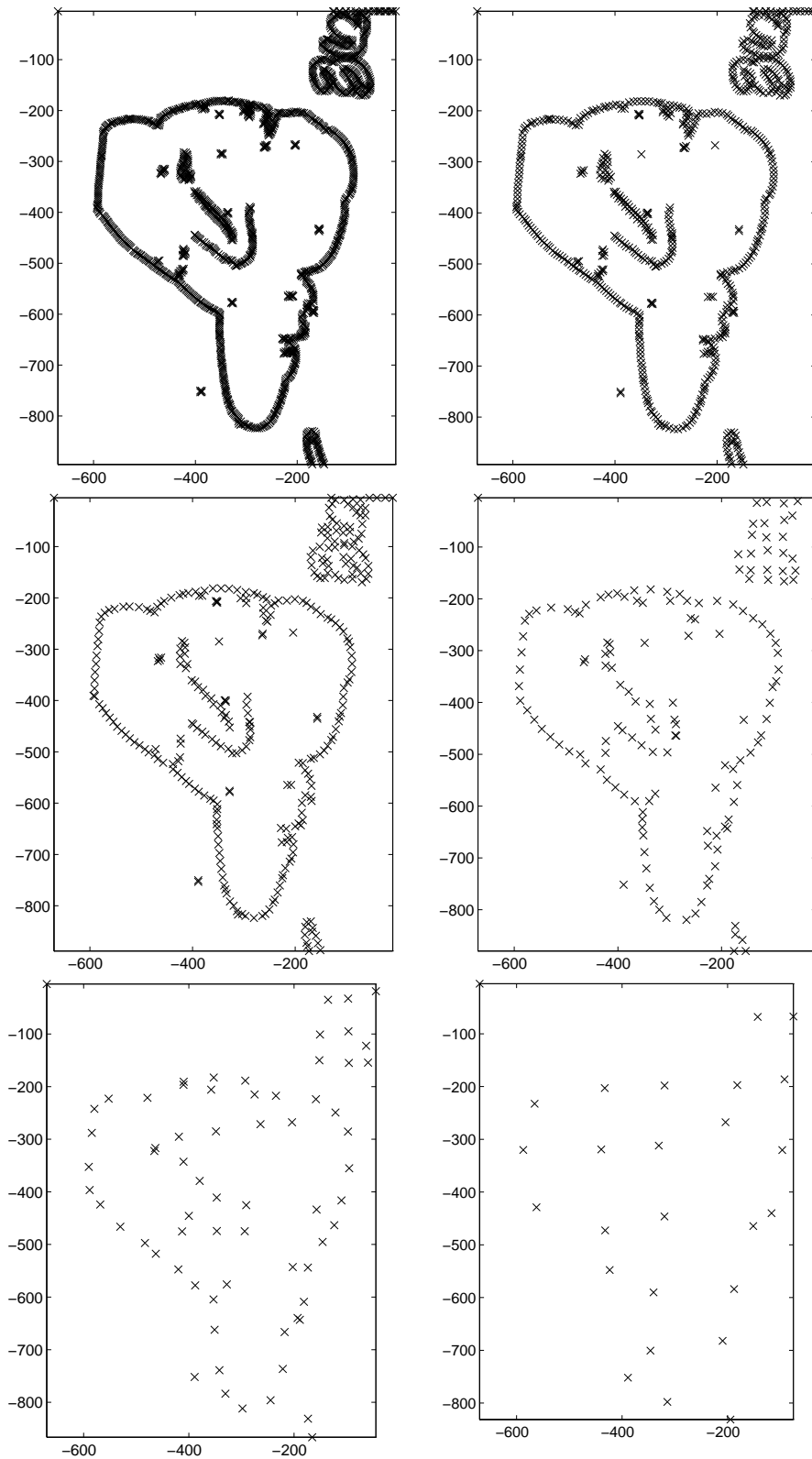


Figure 8: Point-sets from slice 360 obtained at different levels of clustering. From top left to bottom right: clustering levels of 4, 8, 16, 32, 64, 128 with 1351, 669, 327, 152, 68 and 26 points respectively.



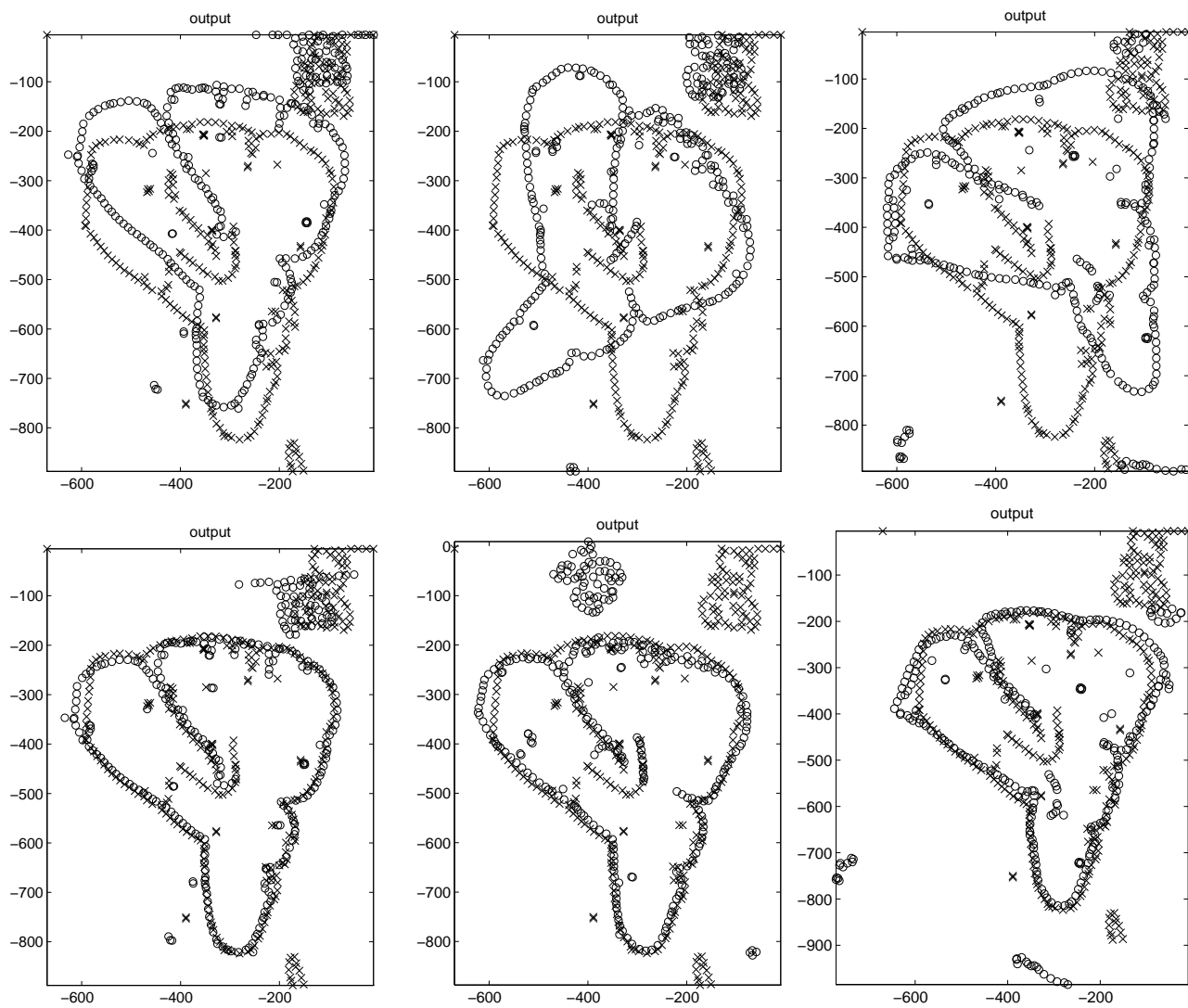


Figure 9: Top: Initial conditions. Left: Slices 360-363, Center: Slices 360-384, Right: Slices 360-415. Bottom: Final solution found by RPM. Left: Slices 360-363, Center: Slices 360-384, Right: Slices 360-415

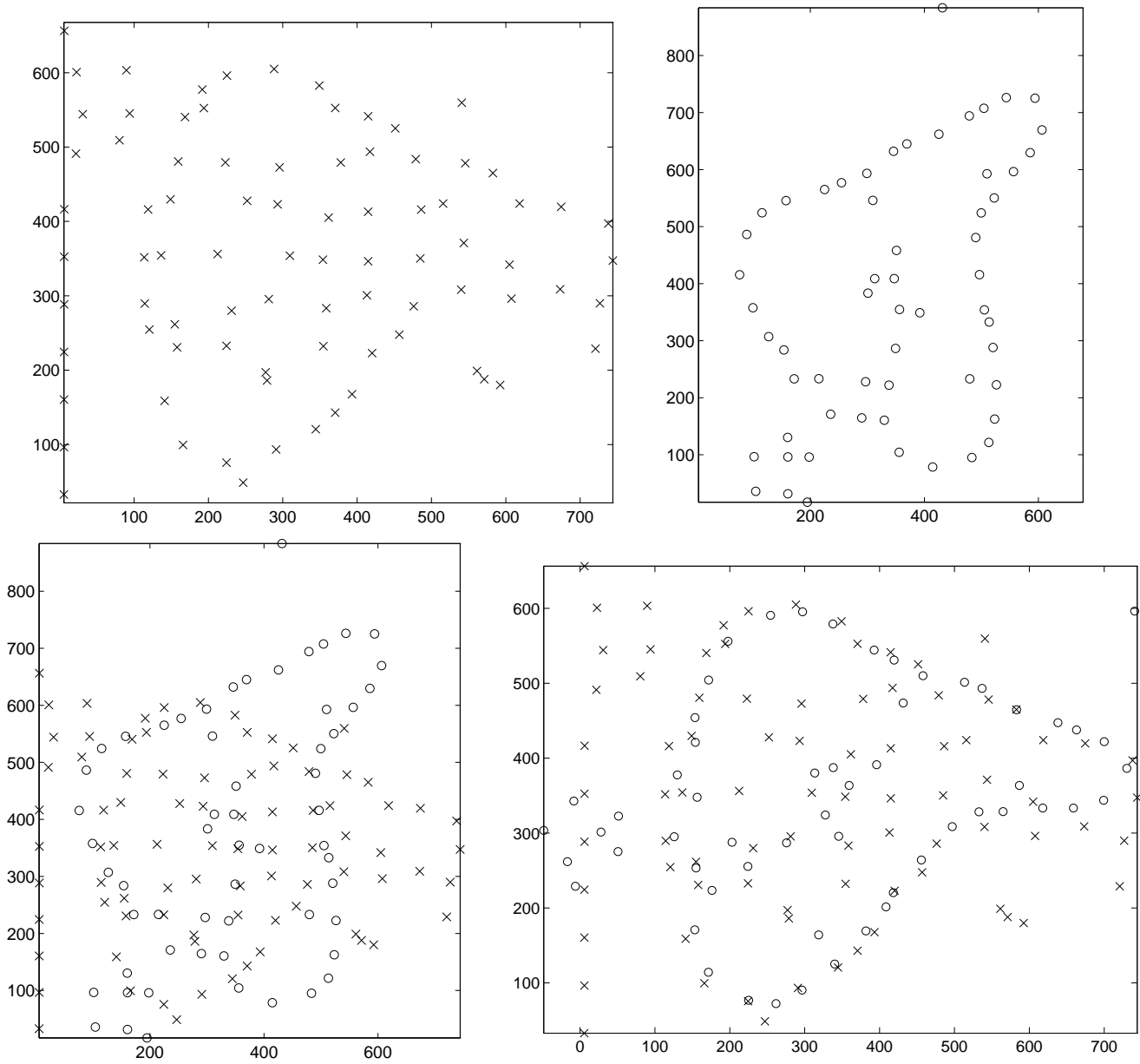


Figure 10: Top Left: Slice 363 with many internal point features. Top Right: Slice 384. Bottom Left: Initial conditions. Bottom Right: Final result showing the good fit between the outer contours of the slices.

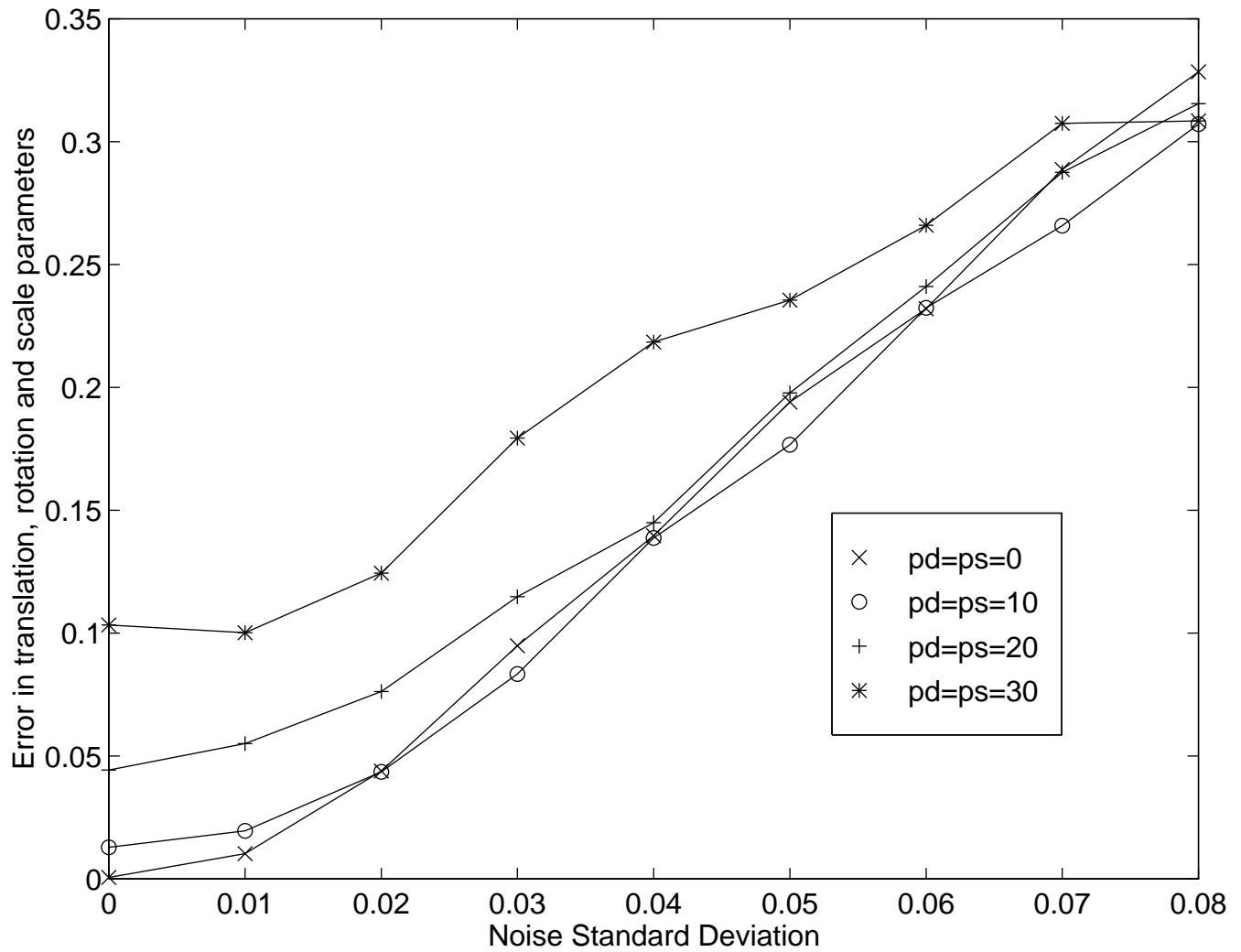


Figure 11: Registration results for the RPM algorithm with synthetically generated transformation parameters.  $p_d$  and  $p_s$  represent the percentages of the deleted and spurious points relative to the original size of the point-set (100 points).

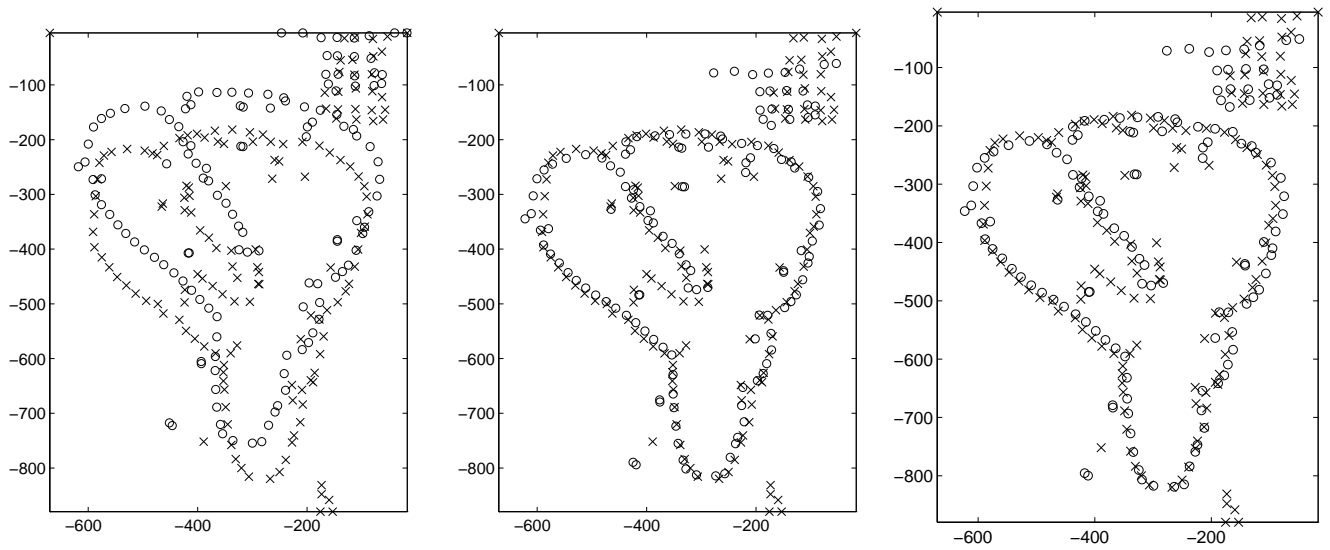


Figure 12: Left: Initial condition for slices 360 and 363. Center: RPM result. Right: ICP result.

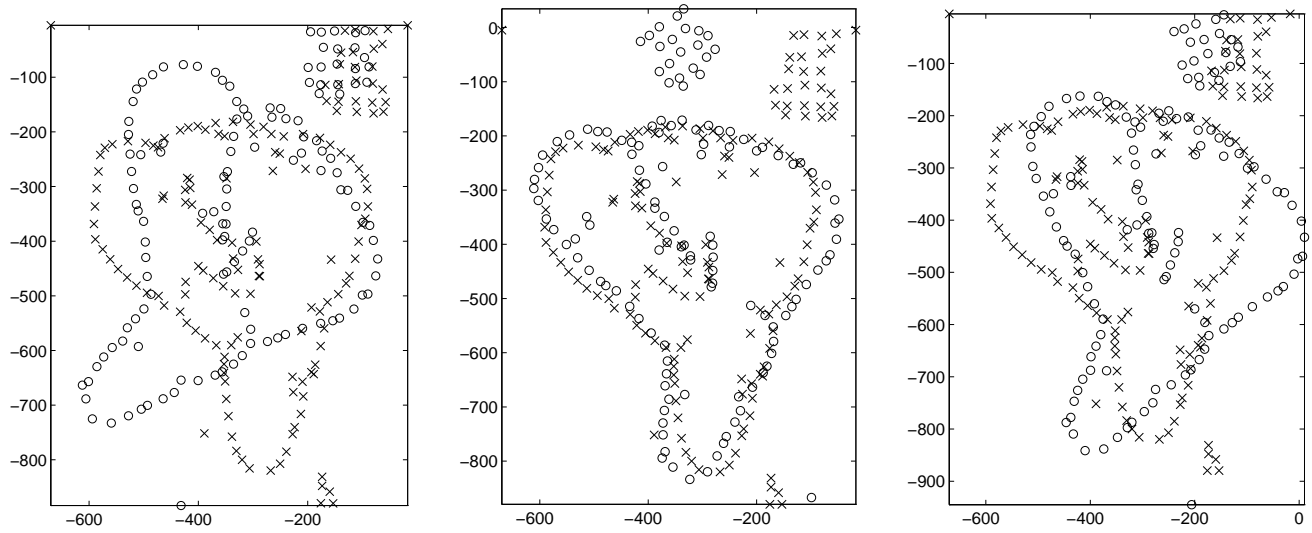


Figure 13: Left: Initial condition for slices 360 and 384. Center: RPM result. Right: ICP result.

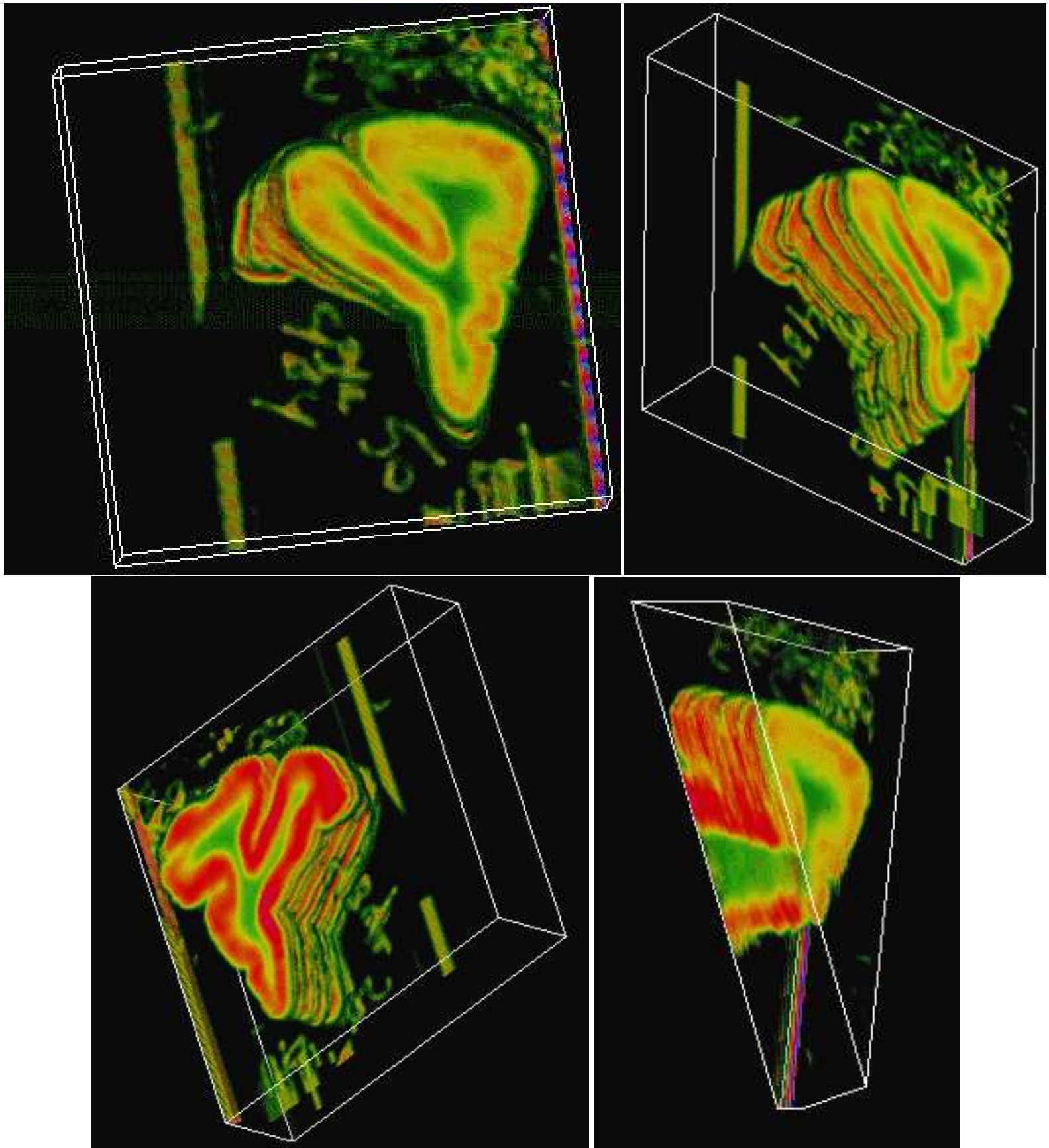


Figure 14: Visualization of the autoradiograph stack.